NANO LETTERS

Letter

pubs.acs.org/NanoLett

Quasi-ballistic Electronic Thermal Conduction in Metal Inverse Opals

Michael T. Barako,[†] Aditya Sood,[†,‡] Chi Zhang,[†] Junjie Wang,[§] Takashi Kodama,[†] Mehdi Asheghi,[†] Xiaolin Zheng,[†] Paul V. Braun,[§] and Kenneth E. Goodson*[,†]

[†]Department of Mechanical Engineering, [‡]Department of Materials Science and Engineering, Stanford University, Stanford, California 94305, United States

[§]Department of Materials Science and Engineering and Frederick Seitz Materials Research Laboratory, University of Illinois at Urbana−Champaign, Urbana, Illinois 61801, United States

Supporting Information

ABSTRACT: Porous metals are used in interfacial transport applications that leverage the combination of electrical and/or thermal conductivity and the large available surface area. As nanomaterials push toward smaller pore sizes to increase the total surface area and reduce diffusion length scales, electron conduction within the metal scaffold becomes suppressed due to increased surface scattering. Here we observe the transition from diffusive to quasi-ballistic thermal conduction using metal inverse opals (IOs), which are metal films that contain a periodic arrangement of interconnected spherical pores. As the material dimensions are reduced from ∼230 nm to ∼23 nm, the thermal conductivity of copper IOs is reduced by more than 57% due to the increase in surface scattering. In contrast, nickel IOs exhibit diffusive-like conduction and have a constant thermal conductivity over this size regime. The quasi-ballistic nature of electron transport at these length scales is modeled considering the inverse opal geometry, surface scattering, and grain boundaries. Understanding the characteristics of electron conduction at the nanoscale is essential to minimizing the total resistance of porous metals for interfacial transport applications, such as the total electrical resistance of battery electrodes and the total thermal resistance of microscale heat exchangers.

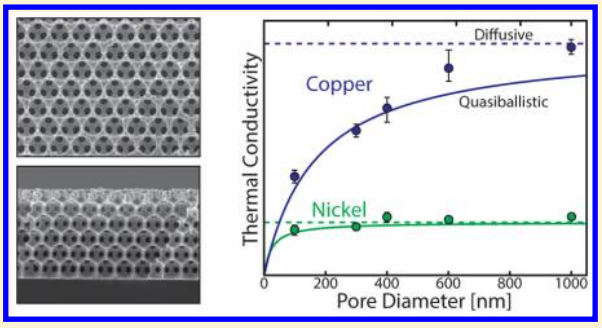

KEYWORDS: *Inverse opal, thermal conductivity, electron scattering, porous metal, surface scattering*

Porous metals uniquely combine a continuous conductive scaffold with a tunable porous morphology for enhanced interfacial transport in applications ranging from electrochemical surfaces[1,2] to microscale heat exchangers.[3] The total thermal and electrical resistance of a porous metal used for interfacial transport is comprised of the conduction resistance in the metal and the transport resistance across the interface. For example, in microscale heat exchangers the high thermal conductivity metal spreads heat and maximizes the thermally accessible porous volume to leverage the large available surface area for heat transfer across the solid−fluid interface. The surface properties of a porous medium depend on the absolute dimensions of the porous material, and many interfacial transport applications, such as convective heat transfer, favor reduced pore sizes to increase the specific surface area and to decrease diffusion lengths. In contrast, the conductivity of a porous metal is only a function of the material composition and the relative geometric arrangement of the phases. However, as the characteristic length scale of the dominant conduction pathway is reduced to nanoscale dimensions, electron scattering from the pore surfaces becomes increasingly significant and reduces the effective conductivity. Consequently, there is a trade-off between reducing pore size to enhance interfacial transport and increasing pore size to improve conductivity for nano- and mesoporous metals.

In the present work, we use metal inverse opals having feature sizes down to ∼23 nm to demonstrate the effects of pore size on thermal conduction in a metal inverse opal (IO), which is a metal thin film that contains a lattice of close-packed, interconnected spherical voids. Inverse opals have been used because of their tunable periodicity, diffractive and optical properties, fluid permeability, and high surface area-to-volume ratio for applications including photonic crystals,[4−11] phononic crystals,[12] catalytic surfaces,[13−15] sensors,[16] membranes,[17] supercapacitors,[18] and battery electrodes.[1,2,19−21] Microfluidic heat exchangers are one of the promising thermal applications for metal IOs due to the high thermal conductivity of the metal and the large fluid-accessible surface area, which enables a low total thermal resistance. However, while enhanced phonon surface scattering has been demonstrated in polycrystalline silicon IOs,[12] there has been relatively little work to characterize the effective thermal conductivity of metal IOs.

We directly measure the effective thermal conductivity in both the diffusive and quasi-ballistic regimes for nickel and copper IOs using a version of the 3ω technique. The diffusive conductivity is

Received: February 2, 2016
Revised: March 10, 2016
Published: March 17, 2016

DOI: 10.1021/acs.nanolett.6b00468
Nano Lett. 2016, 16, 2754−2761

shown to agree well with effective medium theory and finite element models, and we observe a suppression of the effective conductivity when the conduction length scales become comparable to the bulk mean free path (MFP) of the electrons. The bulk MFP of conduction electrons in metals ($\sim 10^1$ nm) is generally much shorter and with a narrower distribution than phonons in single crystal semiconductors like Si ($\sim 10^2$–10^3 nm), and therefore the transition to quasi-ballistic conduction occurs at much smaller length scales compared to phonons in crystals.[22−24] Hung et al. measured the change in electrical conductivity of gold IOs with pore size and attributed this suppression to surface scattering for pore sizes below 500 nm.[25] We show that the conduction network in a face-centered cubic (FCC) IO is well-modeled by a series of interconnected space-filling hard spheres that occupy tetrahedral and octahedral interstitial sites in the lattice as shown in Figure 1, and the

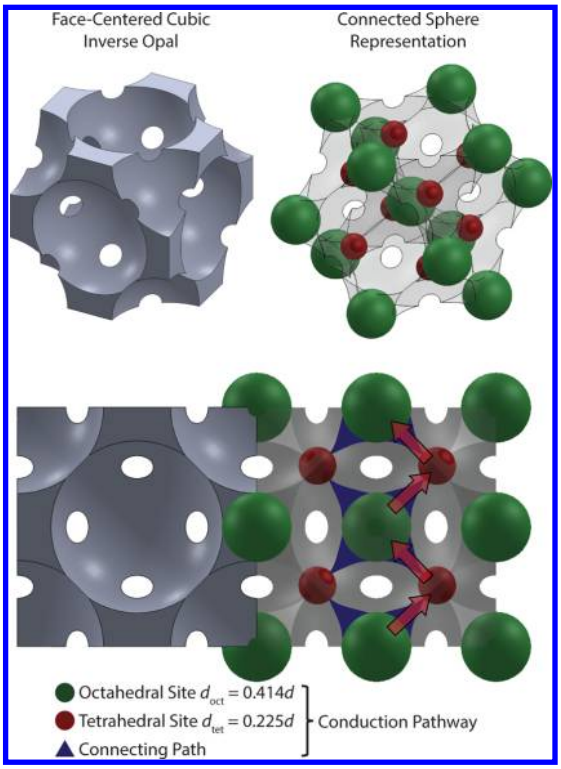

Figure 1. Schematic of a face-centered cubic (FCC) inverse opal unit cell (left) with space-filling spheres located at the characteristic interstitial sites (right). The inverse opal geometry is described by a cubic unit cell containing a FCC arrangement of spherical pores that are connected to the adjacent pores by circular windows. The solid volume is comprised of both octahedral sites (green) and tetrahedral sites (red). The volume of each site can be approximated by space-filling hard spheres that have characteristic diameters relative to the inverse opal pore diameter d. The conduction pathway in an inverse opal (indicated by red arrows) can be represented by a network of interstitial spheres connected by continuous linkages (blue).

diameter of these spheres provides a simple estimate for a characteristic conduction length scale. The following work demonstrates the accuracy of this model through more rigorous calculation of the conduction length scale in a FCC IO by solving the complete volume-averaged integral. This model suggests that the tetrahedral sites are the primary constriction for conduction electrons. Since both thermal and electrical conduction in a metal are governed by the same electron transport physics in an equivalency described by the Wiedemann−Franz Law, the size effect scaling of thermal conductivity is expected to also apply to the electrical conductivity.

Inverse opals are formed by templated deposition, where the IO material is deposited into the interstitial spaces of a sacrificial opal template, which is a close-packed, periodic arrangement of monodisperse spheres. After removing the opal template, the resulting IO is comprised of a continuous scaffold containing a periodic arrangement of interconnected spherical pores. The porosity can be tuned either through modifying the opal template (e.g., sintering the opal) or through postfabrication material processing (e.g., electropolishing). Sacrificial opal templates can be self-assembled from both SiO_2[4−7,12,26−29] and polymer[1,2,8,13−16,18,19,30−36] spheres having diameters as small as one hundred nanometers and as large as several microns. These spheres are self-assembled into close-packed opals using spin coating,[28] vertical deposition,[1,2,5,8,26,27,29,33−35] sedimentation,[4,13,30] and flow cells.[31,32] The opal quality and geometric properties (e.g., pore size, window size, opal thickness) can be tuned through the self-assembly parameters, including the sphere diameter, sphere concentration, solvent evaporation rate, and annealing conditions. There are comprehensive reviews of opal self-assembly methods and the governing physics available in the literature.[9,10,37] Different materials have been used to form the IO including metals,[1,2,7,8,14,18,20,27,31] semiconductors,[4,5,12] polymers,[6,15−17,32,34] and oxides,[13,19,30,33,35,36] and these materials can be deposited using electrodeposition,[1,2,8,14,18−20,31] electroless deposition,[27] chemical vapor deposition,[4,5,12] and capillary infiltration.[7,13,15,16,30,32−35] Opals and IOs have been grown as thick as 100 μm[31] and over areas as large as a 4-in. silicon wafer.[28]

In the present work, metal IOs are fabricated using electrodeposition into polystyrene opal templates, where the sacrificial template (i.e., the opal) defines the resulting morphology of the electrodeposited metal (i.e., the inverse opal). The opal template is synthesized using an adaptation of the convective vertical deposition technique (Figure 2a−f) described by Yu et al.[8] In this method, a hydrophilic metal-coated substrate is placed vertically into a heated well that contains a suspension of nanospheres. As the solvent evaporates, the edge of the meniscus travels along the surface of the substrate and the nanospheres are pulled into a crystal by capillary forces. After drying, the opal is annealed to improve the integrity of the crystal by fusing adjacent spheres together; these points of contact determine the window size connecting adjacent pores in the IO. The opal is then used as a template for electrodeposition of both nickel and copper IOs, where the metal is deposited into the interstitial spaces between the spheres beginning at the substrate surface (Figure 2g). Galvanostatic (i.e., constant current) electrodeposition is performed in a three-electrode cell using the electrochemical parameters given in the Supporting Information. After the metal is deposited, the substrate is placed in tetrahydrofuran to dissolve the polystyrene spheres (Figure 2h). The resulting IO contains a large-grained FCC crystalline array of interconnected, monodisperse pores as shown in Figure 2i. The pore size of each IO is determined by the diameter of the nanospheres in the opal, which are selected to produce IOs having pore sizes ranging from 100 to 1000 nm (Figure 3). The thickness of the IO is determined by the electrodeposition time and can be as large as the thickness of the opal template. A more detailed description of the opal self-assembly and IO synthesis can be found in the Methods section and the Supporting Information.

We measure the effective thermal conductivity of the IOs using the 3ω method,[38−42] which is an electrothermal frequency-

DOI: 10.1021/acs.nanolett.6b00468
Nano Lett. 2016, 16, 2754−2761

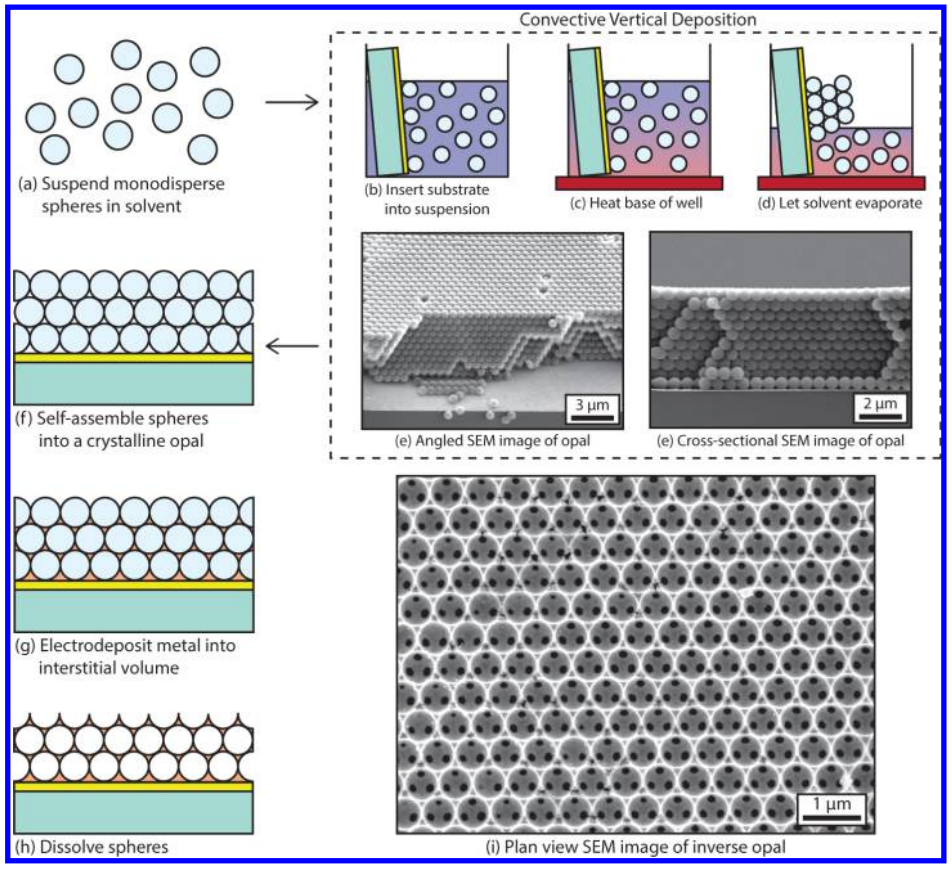

Figure 2. Overview of metal inverse opal synthesis. (a) Sulfate-terminated polystyrene spheres are suspended in deionized water and self-assembled into a close-packed opal using convective vertical deposition. (b) The substrate is placed vertically into a well filled with the sphere suspension. (c) The base of the well is heated to induce convective currents within the suspension to provide gentle mixing. (d) As the solvent evaporates, the meniscus travels along the length of the substrate, pulling the spheres into a close-packed crystal. (e,f) The resulting opals are crystalline and with a well-defined number of layers as demonstrated via scanning electron microscopy (SEM). (g) Metal is then electrodeposited into the interstitial volume, beginning at the substrate, to form the inverse opal. (h) The opal template is then dissolved to form the inverse opal, which is characterized by a crystal of spherical pores (with diameters equal to the diameter of the polystyrene spheres) that are connected by interpore windows. (i) This is shown for a representative nickel inverse opal having pore diameter 600 nm using SEM imaging.

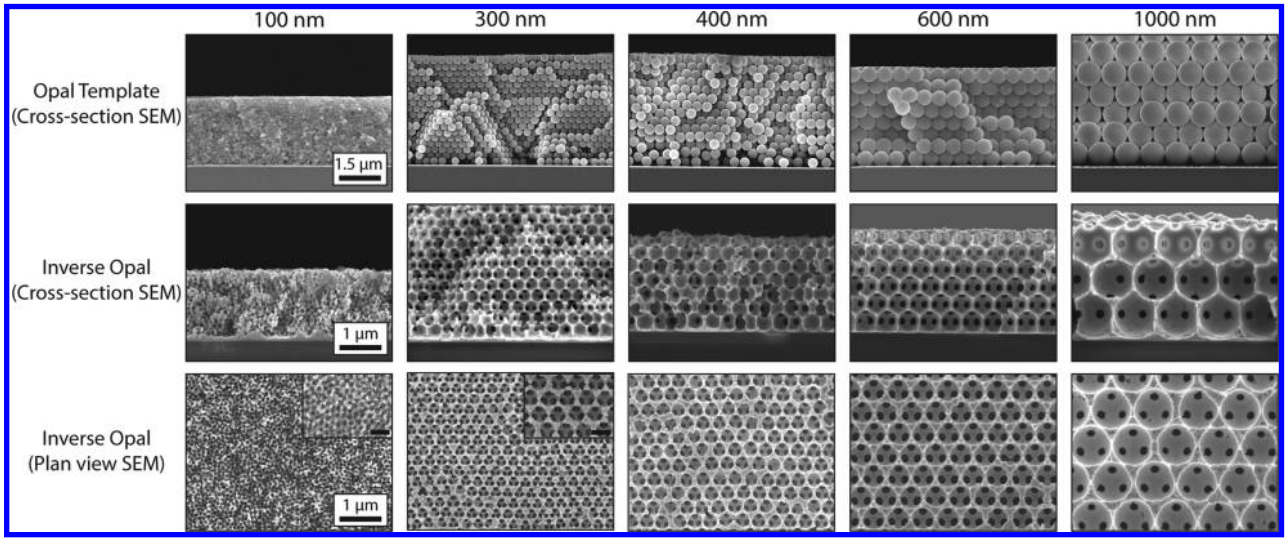

Figure 3. Representative scanning electron micrographs of opals and inverse opals fabricated and studied in the present work having pore diameters ranging from 100 to 1000 nm. This includes cross-sectional images of the opal template (top row) and nickel inverse opals (middle row) as well as plan view images of the nickel inverse opals (bottom row). These films range from 2 to 8 μm in thickness. The scale bars in the inset plan view SEM images are 300 nm.

domain measurement that uses a single metal line to simultaneously generate Joule heating and detect the corresponding temperature rise. In brief, the metal line is driven by a current at frequency ω to generate Joule heating and temperature

DOI: 10.1021/acs.nanolett.6b00468
Nano Lett. 2016, 16, 2754−2761

oscillations at frequency 2ω. The linear relationship between temperature and resistance in a metal causes resistance fluctuations at frequency 2ω, which are detected by a voltage at frequency 3ω. We implement this method using a previously reported[43] measurement configuration and microfabricated device structure, where the IO is synthesized directly above an electrically passivated heater/thermometer device on a fused silica substrate (see Figure 4). The driving current is chosen to

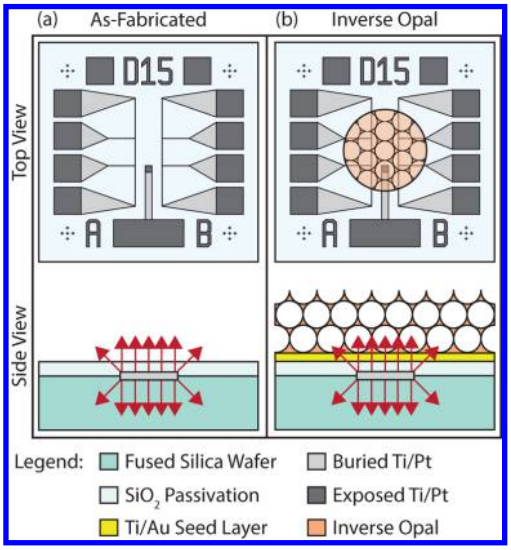

Figure 4. (a) Top and side view of electrically passivated 3ω thermal characterization devices immediately following microfabrication. (b) Top and side view of the same devices after metal seed layer and inverse opal deposition. A more detailed description of these devices is available in the literature.[43]

adjust the temperature rise seen at the heater to ~1 K, which provides a large signal-to-noise ratio without sensing any temperature-dependent thermal properties or requiring consideration of nonlinear Joule heating in the metal line. The detailed preparation of IO synthesis on microfabricated devices is described in the Supporting Information.

The measured voltage signal at the third harmonic $V_{3\omega}$ is mapped to the spatially averaged temperature rise in the heater ΔT_{exp}:[39]

$$\Delta T_{exp} = \frac{2V_{3\omega}(dT/dR)}{I_{RMS}} \tag{1}$$

where dT/dR corresponds to the measured linear relationship between temperature and resistance in the metal line and I_{RMS} is the root-mean-squared current. The temperature oscillations at the heater are a function of the thermal properties of the surrounding materials located approximately within the thermal penetration length $L_{thermal} \approx \sqrt{\alpha/\omega}$ of the heater, where α is the effective thermal diffusivity of the system. The unknown thermal properties of the multilayered stack (see Figure 4) are extracted using a least-squares fitting algorithm to compare the measured thermal frequency response $\Delta T_{exp}(\omega)$ to the analytical heat diffusion equation over the measurement frequency range (200–3000 Hz in the present work). The spatially averaged temperature rise $\Delta T(\omega)$ at the location of heating for a multilayered system is derived[40,44] to be

$$\Delta T = \frac{P}{2\pi L b^2}\int_0^\infty \frac{B^+(m)+B^-(m)}{A^+(m)B^-(m)-A^-(m)B^+(m)} \times \frac{\sin^2(mb)}{\gamma_j m^2}dm \tag{2a}$$

$$\gamma_j = k_j\sqrt{m^2 - i\frac{\omega}{\alpha_j}} \tag{2b}$$

where P is the heating power, L and b are the length and half-width of the heater, respectively, k_j and α_j are the thermal conductivity and diffusivity of the j^{th} layer, and A and B are dimensionless parameters solved using a recursive matrix method. For the IO thermal property measurement, the effective isotropic thermal conductivity and heat capacity of the inverse opal layer are used as fitting parameters, while the thickness is determined independently using cross-sectional scanning electron microscopy. The IO is treated as an effective medium (i.e., spatially homogeneous properties) since the thermal penetration length, heater width, and IO film thickness are all large compared to the individual pore diameter. The measurement configuration in the present work is uniquely sensitive to both the effective thermal conductivity k_{eff} and the heat capacity $C_{v,eff}$ of the IO over the selected frequency range (see Supporting Information); this enables the independent extraction of both k_{eff} and $C_{v,eff}$ using a simultaneous multiparameter fit.

The composite properties of porous media are commonly modeled using effective medium theory (EMT), where a multicomponent composite is treated as a homogeneous material with a single set of effective properties. These models contain parameters corresponding to the composition of the composite and the geometric arrangement of the components. In a binary porous medium (i.e., one solid phase and one porous phase), the composition is equivalently described by either the solid volume fraction $0 < \Phi < 1$ or the porosity $\varepsilon = 1 - \Phi$, and the geometric arrangement defines the functional form of the effective property relation. When the porous volume has a negligible thermal conductivity compared to the solid component, the anisotropic limit of the effective thermal conductivity $k_{eff,VF}$ for one-dimensional conduction scales linearly with the thermal conductivity of the solid component k_{solid} and the solid volume fraction Φ:

$$k_{eff,VF} = k_{solid}\Phi \tag{3}$$

This is equivalent to modeling the two components as parallel resistors and denotes the boundary in the design space of porous media. However, the three-dimensional conduction pathway in an IO is both isotropic and tortuous, and the effective thermal conductivity is reduced relative to eq 3 due to macroscopic bending of the heat flux vectors and the subsequent increase in conduction path length. Maxwell presents an EMT expression for conduction in a solid matrix that contains a uniform but dilute arrangement of spherical pores:[45,46]

$$k_{eff,maxwell} = k_{solid}\left(\frac{2\Phi}{3-\Phi}\right) \tag{4}$$

Datta et al. show that Maxwell's model closely agrees with more comprehensive EMT models for FCC crystals of spherical pores with volume fractions that approach the close-packed limit.[47] A more detailed treatment of EMT conduction models for porous media is compiled by Aichlmayr and Kulacki.[46] While EMT is often used to predict scaling laws for composite media having an

DOI: 10.1021/acs.nanolett.6b00468
Nano Lett. 2016, 16, 2754–2761

unknown arrangement of phases or stochastically distributed porosity, the well-defined and periodic geometry of a IO can be more accurately modeled using finite element analysis. By varying the ratio of pore diameter to unit cell size, the effective thermal conductivity is extracted for a range of solid volume fractions, including the close-packed limit (Φ_{IO} = 0.26) and approaching the minimum required volume fraction for a continuous solid phase ($\Phi_{IO,min}$ = 0.036).[1] The finite element model demonstrates that Maxwell's model overpredicts the effective conductivity for close-packed and high-porosity inverse opals but agrees to within 5% for low porosity ε < 0.65 (or equivalently Φ > 0.35) as shown in Figure 5a. In the diffusive limit, the thermal conductivity of a close-packed FCC inverse opal (Φ_{IO} = 0.26) is independent of pore size with a value of $k_{IO,diff} \approx 0.16 k_{solid}$, which is representative of the FCC IOs synthesized in the present work.

As the pore diameter d is reduced to submicron length scales, there is an increase in surface scattering of the conduction energy carriers within the IO; this effect becomes significant when the geometric conduction length scale approaches the diffusive MFP Λ_{diff} of the energy carriers (e.g., Λ_{diff} = 39 nm for electrons in copper at room temperature,[48,49] see Supporting Information). The surface-limited MFP $\Lambda_{surface}$ (i.e., the ballistic limit) for a close-packed FCC IO unit cell is approximated by computing the mean distance from all points of origin $\vec{r}_o$ in the solid volume to all possible line-of-sight surface points:

$$\Lambda_{surface} = \frac{1}{V}\oint_V \left[\frac{1}{4\pi}\int_\phi\int_\theta L(\vec{r}_o, \theta, \phi)\sin\theta \, d\theta \, d\phi\right] d^3\vec{r}_o \quad (5)$$

where the trajectory of the particle is defined by a polar angle θ and an azimuthal angle φ. This strategy provides an estimate of the electron MFP in a complex, arbitrary geometry using a simplified approach modeled after the canonical Fuchs–Sondheimer formalism for electron surface scattering.[50,51] The integral in eq 5 is numerically computed by considering a finite set of energy carriers with randomly sampled origins in an IO unit cell with periodic boundary conditions. A straight line is drawn from each origin point $\vec{r}_o$ in a randomly selected direction (θ,φ) until it first intersects a pore surface at point $\vec{r}_f$, and the total path length $L(\vec{r}_o, \theta, \varphi) = |\vec{r}_f(\vec{r}_o, \theta, \varphi) - \vec{r}_o|$ is recorded. The surface-limited MFP $\Lambda_{surface}$ is numerically calculated by sampling L for a statistically large ensemble of n points, each having an arbitrary origin and trajectory:

$$\Lambda_{surface} = \lim_{n\to\infty}\left(\frac{1}{n}\sum_{i=1}^{n} L_i\right) \quad (6)$$

The trajectory is defined by a polar angle θ and an azimuthal angle φ that are randomly sampled over all cos(θ) in the domain [−1,1] and φ in the domain [0,2π]. For an FCC IO with pore diameter d and unit cell side length a, eq 6 converges to $\Lambda_{surface} \approx 0.165a$ or alternatively $\Lambda_{surface} \approx 0.233d$, which is nearly equal to the tetrahedral site diameter $d_{tet} = 0.225d$ characteristic of an FCC hard sphere model as shown in Figure 1. This approximation has been previously utilized by Hung et al. to model electrical transport in gold inverse opals.[25] This suggests that the conduction pathway in an IO is well-modeled using a series of interconnected spheres centered at the interstitial sites. Quasi-ballistic conduction is primarily limited by the tetrahedral sites, which are the smaller of the two types of interstitial sites.

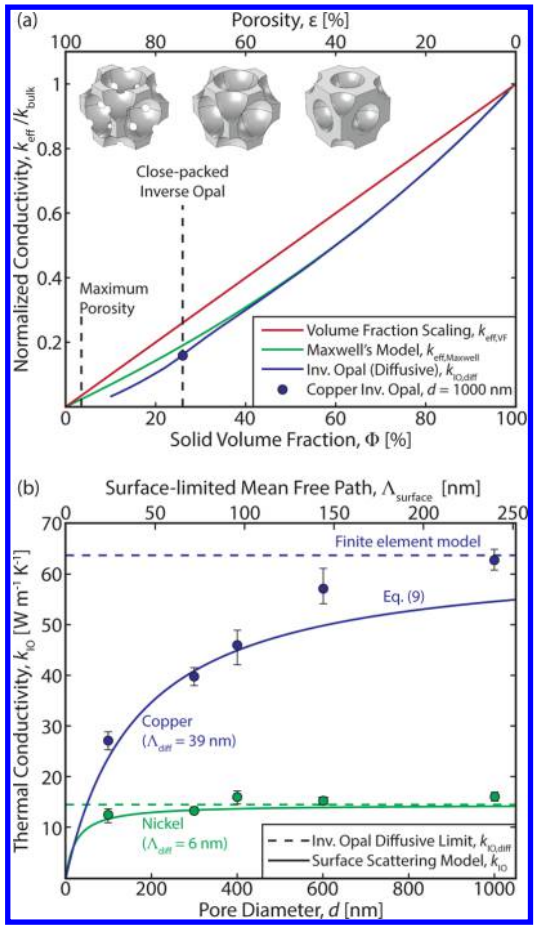

Figure 5. (a) Thermal conductivity scaling with volume fraction in the diffusive conduction regime. The volume fraction scaling (red line) given by eq 3 corresponds to the physical upper bound for a one-dimensional porous medium (i.e., parallel resistors) but overestimates the thermal conductivity of any isotropic porous medium. Maxwell's model (green line) given by eq 4 is an effective medium approximation that accounts for the macroscopic bending of the heat flux around a regular but dilute arrangement of spherical pores. A finite element model (blue line) provides a more accurate prediction of thermal conductivity for an exact FCC arrangement of spherical pores in a solid matrix, which agrees well with the data. (b) Thermal conductivity scaling with pore diameter for close-packed inverse opals (Φ_{IO} = 0.26) in the quasi-ballistic conduction regime. For large pores, the thermal conductivity is independent of pore size and converges to the diffusive limit (dashed lines). As the pore size is reduced, the geometric length scales of the inverse opal become comparable to the mean free path of the energy carriers, which results in increased surface scattering and a reduced effective thermal conductivity (solid lines) described by eq 9. Experimental data are shown for copper (blue) and nickel (green) inverse opals.

The diffusive electron MFP Λ_{diff} of a polycrystalline metal can be reduced by grain boundary scattering and other crystal defects, and these effects can be amplified owing to the fabrication details pursued here. The average size of the individual grains d_{GB} has been observed to scale approximately linearly with feature size in nanoscale materials.[12,52] We use X-ray diffraction (XRD) to estimate d_{GB} as a function of template feature size, but we observe negligible changes in d_{GB} between IOs having the largest and smallest pores (see Supporting Information). This can be attributed to grains being smaller than the IO feature size, where grain growth during electrodeposition is only minimally affected by template boundaries. Furthermore,

DOI: 10.1021/acs.nanolett.6b00468
Nano Lett. 2016, 16, 2754−2761

surface oxidation may form over the surface area of the metal IO, though we do not expect the surface oxide to significantly impact the conductivity (see Supporting Information). To minimize the effects of oxygen diffusion into the metal, all thermal measurements are conducted within 1 h of IO synthesis.

The combined effects of surface scattering and internal scattering (e.g., electron−phonon, electron−grain boundary) in an IO are modeled by an effective MFP Λ_{IO} using Matthiessen's rule:

$$\Lambda_{IO} = \left[\frac{1}{\Lambda_{diff}} + \frac{1}{\Lambda_{surface}}\right]^{-1} \quad (7)$$

Kinetic theory defines a linear relation between the thermal conductivity and the MFP of the energy carriers under the gray approximation, which is reasonable since electrons in metals have a narrow MFP distribution with energy.[22] A thermal conductivity reduction function is given by combining the results of eq 6 with the expression given by eq 7:

$$\frac{k_{IO}}{k_{IO,diff}} = \frac{\Lambda_{IO}}{\Lambda_{diff}} = \frac{0.233d}{0.233d + \Lambda_{diff}} \quad (8)$$

The total thermal conductivity of an inverse opal k_{IO} is then expressed by scaling the diffusive IO thermal conductivity $k_{IO,diff} \approx 0.16k_{solid}$ determined from the finite element model with the reduction function given by eq 8:

$$k_{IO} = \frac{0.233d}{0.233d + \Lambda_{diff}}(0.16k_{solid}) \quad (9)$$

For $d \gg \Lambda_{diff}$, eq 9 converges to the diffusive limit $k_{IO,diff}$. The effective thermal conductivity scaling with pore size is shown in Figure 5b.

Experimental data are obtained for both copper and nickel inverse opals having pore diameters from 100 to 1000 nm. We implement the Drude−Sommerfeld model to estimate Λ_{diff} for electrons in both copper and nickel at 293 K, which yields $\Lambda_{diff,Cu}$ = 39 nm and $\Lambda_{diff,Ni}$ = 6 nm, respectively (see Supporting Information). This is consistent with values reported in the literature.[53] For the largest pore size (d = 1000 nm), the measured thermal conductivity for both copper and nickel aligns with the diffusive limit $k_{IO,diff}$ from the finite element model. In this regime, $\Lambda_{IO} \approx \Lambda_{diff}$ since the conduction length scales are significantly larger than the MFP of the electrons. Nickel IOs have a short electron MFP and exhibit diffusive-like conduction down to d = 100 nm; we observe an approximately constant conductivity for all nickel IOs in the present work. Copper has a comparatively long electron MFP, and consequently the conductivity monotonically decreases with pore size in this size regime. Our results for copper are consistent with the observed reduction in electrical conductivity by Hung et al.[25] for gold IOs having pore sizes below 500 nm, and the copper IO data agrees well with the surface scattering model given by eq 9. For the copper IO with the smallest pore size (d = 100 nm), the effective thermal conductivity k_{IO} is only 43% of the measured thermal conductivity for d = 1000 nm. In addition, we measure the electrical conductivity (see Supporting Information) of a 100 nm diameter copper IO and observe a reduction in conductivity to ∼40% of the diffusive IO conductivity, which is comparable to the thermal conductivity reduction and consistent with the Wiedemann−Franz law.

Many applications of microscale porous media leverage the large available surface area to enhance the effective interfacial transport properties, which are strong functions of the surface area-to-volume ratio. For a close-packed FCC IO unit cell with pore diameter d and side length $a = d\sqrt{2}$, the surface area-to-volume ratio γ scales with the inverse of the pore diameter:

$$\gamma = \frac{2\pi}{d\sqrt{2}} \quad (10)$$

For both electrochemical and thermofluidic interfacial transport applications of metal IOs, the total resistance is approximated by the sum of the conduction resistance ($\sim 1/k_{IO}$) and the interfacial resistance ($\sim 1/\gamma$). In the diffusive conduction limit, k_{IO} is independent of d and the surface area γ scales with $1/d$; the total resistance is minimized for small pore sizes that maximize the solid−liquid interfacial surface area. However, if the pore size becomes sufficiently small to cause significant surface scattering of the electrons, the dichotomous scaling of conduction resistance ($\sim 1/d$) and interfacial resistance ($\sim d$) with pore size suggests an optimization for minimizing the total resistance. For example, in an electrochemical system (e.g., an IO-based battery electrode[1]) a high electrical conductivity is needed to minimize parasitic voltage drops within the electrode while a large surface area and short diffusion length is needed to maximize electrochemical activity at the electrode−electrolyte interface. In a thermofluidic system (e.g., microfluidic heat exchanger), a high thermal conductivity is needed to spread heat away from the source to maximize the thermally accessible area of the solid−liquid interface. However, the flow fields within an IO exhibit a more complicated dependence on pore size, and the design of an IO-based microfluidic heat exchanger requires more detailed consideration of the flow configuration to accurately predict pressure gradients, heat transfer coefficients, and total convection resistances.

Concluding Remarks. Here we utilize a three-dimensional metal macrostructure ($\sim 10^5$ nm) to demonstrate quasi-ballistic electronic thermal transport properties from a high-density network of nanoscale features ($\sim 10^2$ nm). This finding is consistent with our model for enhanced surface scattering along the principal conduction pathway in a FCC inverse opal. The size-effect scaling of thermal conductivity also describes the electrical conductivity scaling of metal inverse opals, which is important for electrical and electrochemical applications. Engineering the thermal conductivity of a porous metal is the first critical step in the design of microscale heat exchangers and enhanced heat transfer surfaces. Conduction in the porous metal spreads heat from the source throughout the porous volume to leverage the large available solid−fluid interfacial area. Another set of critical factors are defined by the properties of the porous volume, which determines the efficacy of heat transfer across the solid−fluid interface. A full heat exchanger analysis additionally requires consideration of heat transfer coefficients and hydraulic parameters such as fluid permeability and capillary pressure. While IOs represent an important class of porous morphologies, the conduction principles outlined here can be adapted to describe conduction in other porous metals containing nanoscale feature sizes, such as sintered copper, woodpile scaffolds, or nanowire networks.

Methods. *Opal Self-Assembly by Convective Vertical Deposition.* In the present work, crystalline FCC opals are prepared by convective vertical deposition.[8] An aqueous suspension of sulfate-terminated polystyrene spheres (Life Technologies Corporation) is diluted to 0.4% w/v and sonicated for 15 min to disperse the spheres. A substrate is prepared by depositing a metal seed layer (5 nm Ti + 50 nm Au) onto the

DOI: 10.1021/acs.nanolett.6b00468
Nano Lett. 2016, 16, 2754−2761

surface using electron beam evaporation through a shadow mask to pattern the seed layer. The substrate is immersed in 1 mM aqueous sodium 3-mercapto-1-propanesulfonate for a minimum of 24 h to form a self-assembled monolayer that renders the Au surface hydrophilic. Convective vertical deposition is performed in a tissue culture plate (Corning Inc.) containing a 48-well array of individual 9 mm diameter and 20 mm deep cylindrical wells. A copper plate is affixed using thermal grease to the bottom of the culture plate as a heat spreader to ensure temperature uniformity across all of the wells. The culture plate is placed on a hot plate in ambient air, and the temperature is adjusted until the base of the well is at 50−55 °C (measured by a thermocouple at the base of the well). The substrate is then placed vertically into a well, and 0.5 mL of nanosphere suspension is transferred into the well via pipet. As the solvent evaporates (∼12 h), the edge of the meniscus travels along the surface of the substrate, and the nanospheres are pulled into a crystal by capillary forces. The heated base is used to induce convective mixing to prevent sedimentation of the spheres and to replenish spheres at the edge of the meniscus as they are pulled out of suspension and into the opal. The opal is then annealed in an oven at 95 °C for 5 h (1 h for 100 nm-diameter spheres) to sinter adjacent spheres together and to enhance the cohesiveness of the crystal. Increasing the sintering time and/or temperature increases the degree of connectivity and increases the interpore window size.

Electrodeposition of Inverse Opal. Metal is electrochemically deposited into the interstitial volume of the opal template using galvanostatic electrodeposition. The substrate is prepared by affixing a PTFE-coated wire to the buried working electrode using colloidal silver paint (Electrodag 1415, Ted Pella Inc.), and the connection is covered with epoxy (5 min Epoxy, Devcon Inc.) to prevent electrodeposition onto the point of attachment. A three-electrode electrochemical cell is set up in a 50 mL glass beaker with a large area (∼10 cm^2) counter electrode placed vertically on one side of the beaker. It is critical to properly wet the opal to ensure complete infiltration of plating solution and therefore uniform inverse opal coverage (see Supporting Information). After wetting the opal, the substrate is immediately placed into the electrolyte bath on the opposite side of the beaker such that the working electrode is separated from the counter electrode by ∼2 cm. The reference electrode (Ag/AgCl, BaSi Inc.) is suspended over the center of the beaker. Galvanostatic (i.e., constant current) electrodeposition is performed over the total seed layer area of 0.07 cm^2, and the effective current density is given by the total current over the total seed layer area. The true current density will be larger since a significant fraction of the working electrode is masked by the opal template. In the limit of uniform electrodeposition, the exposed working electrode area varies with depth into the opal, and this causes a time-dependent current density as observed by an oscillating voltage signal with deposition time (see Supporting Information). The inverse opal thickness is chosen to contain a minimum of 6 layers of pores as tuned by the total electrodeposition time, which corresponds to 2−8 μm-thick inverse opals. After electrodeposition, the sample is placed in two sequential baths of tetrahydrofuran at 40 °C for 1 h each to dissolve the polystyrene spheres, and afterward the sample is rinsed with deionized water and ethanol. For the substrates containing microfabricated thermal characterization devices, additional details of the inverse opal synthesis are available in the Supporting Information.

Thermal Characterization Methodology. The effective thermal conductivity of each inverse opal k_{IO} is measured using a microfabricated substrate implementation of the 3ω method as previously reported.[43] Each heater line is nominally 1000 μm long and 5 μm wide and has a measured resistance that ranges from R = 430−470 Ω at room temperature, which gives a heater sensitivity of dR/dT = 1.17−1.26 Ω/K. All 3ω measurements are performed using a current source (Keithley 6221) over the frequency range 200−3000 Hz with a driving current of 3 mA during calibration and 4−5 mA during the inverse opal measurement. The 3ω voltage signal is isolated using cascaded differential amplifiers (Analog Devices AD8221) and detected using a lock-in amplifier (Stanford Research Systems SR830). Additional details of the thermal conductivity measurement, including the device fabrication, calibration methodology, and sensitivity and uncertainty analyses, are given in the Supporting Information.

Finite Element Model. The diffusive thermal conductivity of an inverse opal $k_{IO,diff}$ is determined using the commercial software package COMSOL. A cubic unit cell is generated with uniform spherical pores arranged in an FCC lattice. Heat transfer is neglected in the pores since the conductivity of the metal inverse structure is much larger than the conductivity of the fluid in the pores. Since an FCC arrangement is isotropic, the thermal conductivity is the same along each of the three principal axes. Adiabatic boundary conditions are imposed on the four lateral sides of the unit cell (since these are symmetry planes), and constant temperature boundary conditions are imposed on the top and bottom surfaces. The effective thermal conductivity is then calculated by numerically computing the equilibrium heat flux for the imposed temperature differential and applying Fourier's law. The pore size is varied while maintaining a constant unit cell side length to sweep solid volume fractions.

■ ASSOCIATED CONTENT

Supporting Information

The Supporting Information is available free of charge on the ACS Publications website at DOI: 10.1021/acs.nanolett.6b00468.

Additional details on inverse opal synthesis and material characterization, sensitivity and uncertainty analysis for the thermal conductivity measurement, surface scattering model parameters, electrical conductivity measurement, and tabulated data (PDF)

■ AUTHOR INFORMATION

Corresponding Author

*E-mail: goodson@stanford.edu.

Notes

The authors declare no competing financial interest.

■ ACKNOWLEDGMENTS

The authors would like to thank Tim English, Woosung Park, and Katherine Chang for assistance with the microfabrication of the thermal characterization devices. The authors would also like to thank Srilakshmi Lingamneni for assistance setting up the COMSOL simulations and Allison Yau for performing transmission electron microscopy imaging. This work was partially funded by the Defense Advanced Research Projects Agency (DARPA) under award number HR0011-13-2-0011. M.T.B. would like to acknowledge government support under and awarded by the United States Department of Defense, Air Force Office of Scientific Research, National Defense Science and Engineering Graduate (NDSEG) Fellowship, 32 CFR 168a.

DOI: 10.1021/acs.nanolett.6b00468
Nano Lett. 2016, 16, 2754−2761

REFERENCES

(1) Zhang, H.; Yu, X.; Braun, P. V. *Nat. Nanotechnol.* **2011**, *6*, 277−281.
(2) Liu, J.; Zhang, H. G.; Wang, J.; Cho, J.; Pikul, J. H.; Epstein, E. S.; Huang, X.; Liu, J.; Braun, P. V. *Adv. Mater.* **2014**, *26*, 7096−7101.
(3) Weibel, J. A.; Garimella, S. V. *Adv. Heat Transfer* **2013**, *45*, 209−301.
(4) Blanco, A.; Chomski, E.; Grabtchak, S.; Ibisate, M.; John, S.; Leonard, S. W.; Lopez, C.; Meseguer, F.; Miguez, H.; Mondia, J. P.; Ozin, G. A.; Toader, O.; van Driel, H. M. *Nature* **2000**, *405* (6785), 437−440.
(5) Vlasov, Y. A.; Bo, X.-Z.; Sturm, J. C.; Norris, D. J. *Nature* **2001**, *414* (6861), 289−293.
(6) Kang, H.; Lee, J. S.; Chang, W. S.; Kim, S. H. *Adv. Mater.* **2014**.
(7) Kim, J.; Aagesen, L. K.; Choi, J. H.; Choi, J.; Kim, H. S.; Liu, J.; Cho, C.-R.; Kang, J. G.; Ramazani, A.; Thornton, K.; Braun, P. V. *Adv. Mater.* **2015**, *27* (31), 4551−4559.
(8) Yu, X.; Lee, Y. J.; Furstenberg, R.; White, J. O.; Braun, P. V. *Adv. Mater.* **2007**, *19* (13), 1689−1692.
(9) Galisteo-López, J. F.; Ibisate, M.; Sapienza, R.; Froufe-Pérez, L. S.; Blanco, Á.; López, C. *Adv. Mater.* **2011**, *23* (1), 30−69.
(10) Braun, P. V. *Chem. Mater.* **2014**, *26* (1), 277−286.
(11) Schroden, R. C.; Al-Daous, M.; Blanford, C. F.; Stein, A. *Chem. Mater.* **2002**, *14* (8), 3305−3315.
(12) Ma, J.; Parajuli, B. R.; Ghossoub, M. G.; Mihi, A.; Sadhu, J.; Braun, P. V.; Sinha, S. *Nano Lett.* **2013**, *13*, 618−624.
(13) Umeda, G. A.; Chueh, W. C.; Noailles, L.; Haile, S. M.; Dunn, B. S. *Energy Environ. Sci.* **2008**, *1* (4), 484−486.
(14) Ben-Ali, S.; Cook, D. A.; Evans, S. A.; Thienpont, A.; Bartlett, P. N.; Kuhn, A. *Electrochem. Commun.* **2003**, *5* (9), 747−751.
(15) Choi, G. H.; Rhee, D. K.; Park, A. R.; Oh, M. J.; Hong, S.; Richardson, J. J.; Guo, J.; Caruso, F.; Yoo, P. J. *ACS Appl. Mater. Interfaces* **2016**, *8*, 3250.
(16) Lee, Y. J.; Braun, P. V. *Adv. Mater.* **2003**, *15* (7−8), 563−566.
(17) Kim, J.-H.; Kim, J.-H.; Choi, K.-H.; Yu, H. K.; Kim, J. H.; Lee, J. S.; Lee, S.-Y. *Nano Lett.* **2014**, *14*, 4438−4448.
(18) Hsia, B.; Kim, M. S.; Luna, L. E.; Mair, N. R.; Kim, Y.; Carraro, C.; Maboudian, R. *ACS Appl. Mater. Interfaces* **2014**, *6*, 18413−18417.
(19) Armstrong, E.; McNulty, D.; Geaney, H.; O'Dwyer, C. *ACS Appl. Mater. Interfaces* **2015**, *7*, 27006−27015.
(20) Wang, J.; Zhou, H.; Nanda, J.; Braun, P. V. *Chem. Mater.* **2015**, *27* (8), 2803−2811.
(21) O'Dwyer, C. *Adv. Mater.* **2016**, DOI: 10.1002/adma.201503973.
(22) Jain, A.; McGaughey, A. J. *Phys. Rev. B: Condens. Matter Mater. Phys.* **2016**, *93* (8), 081206.
(23) Regner, K. T.; Sellan, D. P.; Su, Z.; Amon, C. H.; McGaughey, A. J.; Malen, J. A. *Nat. Commun.* **2013**, *4*, 1640.
(24) Freedman, J. P.; Leach, J. H.; Preble, E. A.; Sitar, Z.; Davis, R. F.; Malen, J. A. *Sci. Rep.* **2013**, *3*, 2963.
(25) Hung, D.; Liu, Z.; Shah, N.; Hao, Y.; Searson, P. C. *J. Phys. Chem. C* **2007**, *111* (8), 3308−3313.
(26) Jiang, P.; Bertone, J. F.; Hwang, K. S.; Colvin, V. L. *Chem. Mater.* **1999**, *11* (8), 2132−2140.
(27) Jiang, P.; Cizeron, J.; Bertone, J. F.; Colvin, V. L. *J. Am. Chem. Soc.* **1999**, *121* (34), 7957−7958.
(28) Jiang, P.; McFarland, M. J. *J. Am. Chem. Soc.* **2004**, *126* (42), 13778−13786.
(29) Wang, L.; Zhao, X. S. *J. Phys. Chem. C* **2007**, *111* (24), 8538−8542.
(30) Chae, W.-S.; Gough, D. V.; Ham, S.-K.; Robinson, D. B.; Braun, P. V. *ACS Appl. Mater. Interfaces* **2012**, *4* (8), 3973−3979.
(31) Eagleton, T. S.; Searson, P. C. *Chem. Mater.* **2004**, *16*, 5027−5032.
(32) Park, S. H.; Xia, Y. *Adv. Mater.* **1998**, *10* (13), 1045−1048.
(33) Hatton, B.; Mishchenko, L.; Davis, S.; Sandhage, K. H.; Aizenberg, J. *Proc. Natl. Acad. Sci. U. S. A.* **2010**, *107* (23), 10354−10359.
(34) Zhang, X.; Blanchard, G. J. *ACS Appl. Mater. Interfaces* **2015**, *7*, 6054−6061.
(35) Zhou, M.; Bao, J.; Xu, Y.; Zhang, J.; Xie, J.; Guan, M.; Wang, C.; Wen, L.; Lei, Y.; Xie, Y. *ACS Nano* **2014**, *8*, 7088−7098.
(36) Nan, F.; Kang, Z.; Wang, J.; Shen, M.; Fang, L. *Appl. Phys. Lett.* **2015**, *106* (15), 153901.
(37) Yang, S.-M.; Jang, S. G.; Choi, D.-G.; Kim, S.; Yu, H. K. *Small* **2006**, *2* (4), 458−475.
(38) Dames, C.; Chen, G. *Rev. Sci. Instrum.* **2005**, *76* (12), 124902.
(39) Cahill, D. G. *Rev. Sci. Instrum.* **1990**, *61* (2), 802−808.
(40) Kim, J. H.; Feldman, A.; Novotny, D. *J. Appl. Phys.* **1999**, *86* (7), 3959.
(41) Tong, T.; Majumdar, A. *Rev. Sci. Instrum.* **2006**, *77* (10), 104902.
(42) Bauer, M. L.; Norris, P. M. *Rev. Sci. Instrum.* **2014**, *85* (6), 064903.
(43) Barako, M. T.; Roy-Panzer, S.; English, T. S.; Kodama, T.; Asheghi, M.; Kenny, T. W.; Goodson, K. E. *ACS Appl. Mater. Interfaces* **2015**, *7* (34), 19251−19259.
(44) Feldman, A. *High Temp. - High Pressures* **1999**, *31*, 293−298.
(45) Maxwell, J. C. *A Treatise on Electricity and Magnetism*. 3 ed.; Oxford University Press: Oxford, 1892; Vol. *1*.
(46) Aichlmayr, H. T.; Kulacki, F. A. *Adv. Heat Transfer* **2006**, *39*, 377−460.
(47) Datta, S.; Chan, C. T.; Ho, K. M.; Soukoulis, C. M. *Phys. Rev. B: Condens. Matter Mater. Phys.* **1993**, *48* (20), 14936−14943.
(48) Zhang, W.; Brongersma, S. H.; Richard, O.; Brijs, B.; Palmans, R.; Froyen, L.; Maex, K. *Microelectron. Eng.* **2004**, *76* (1−4), 146−152.
(49) Ashcroft, N. W.; David, M. N. *Solid state physics*; Thomson Learning: South Melbourne, 1976.
(50) Fuchs, K. *Math. Proc. Cambridge Philos. Soc.* **1938**, *34* (01), 100−108.
(51) Sondheimer, E. H. *Adv. Phys.* **1952**, *1* (1), 1−42.
(52) Kim, T. H.; Zhang, X. G.; Nicholson, D. M.; Evans, B. M.; Kulkarni, N. S.; Radhakrishnan, B.; Kenik, E. A.; Li, A. P. *Nano Lett.* **2010**, *10* (8), 3096−100.
(53) Gall, D. *J. Appl. Phys.* **2016**, *119* (8), 085101.

DOI: 10.1021/acs.nanolett.6b00468
Nano Lett. 2016, 16, 2754−2761